Experimental characterization of the Clear-PEM scanner spectrometric performance

2009 JINST 4 P10011

(http://iopscience.iop.org/1748-0221/4/10/P10011)

PUBLISHED BY IOP PUBLISHING FOR SISSA
RECEIVED: *July 8, 2009*
ACCEPTED: *September 28, 2009*
PUBLISHED: *October 27, 2009*

Experimental characterization of the Clear-PEM scanner spectrometric performance

R. Bugalho,[a] B. Carriço,[a] C.S. Ferreira,[a] M. Frade,[a,1] M. Ferreira,[a] R. Moura,[a] C. Ortigão,[a] J.F. Pinheiro,[a] P. Rodrigues,[a] I. Rolo,[a] J.C. Silva,[a] A. Trindade[a] and J. Varela[a,b,c]

[a] *Laboratório de Instrumentação e Física Experimental de Partículas (LIP), Av. Elias Garcia 14-1, 1000-149 Lisboa, Portugal*
[b] *Instituto Superior Técnico (IST) da Universidade Técnica de Lisboa, Av. Rovisco Pais, 1049-001 Lisboa, Portugal*
[c] *European Organization for Nuclear Research (CERN), CH-1211 Genève 23, Switzerland*
E-mail: frade@lip.pt

ABSTRACT: In the framework of the Clear-PEM project for the construction of a high-resolution and high-specificity scanner for breast cancer imaging, a Positron Emission Mammography tomograph has been developed and installed at the *Instituto Português de Oncologia do Porto* hospital. The Clear-PEM scanner is mainly composed by two planar detector heads attached to a robotic arm, trigger/data acquisition electronics system and computing servers. The detector heads hold crystal matrices built from $2 \times 2 \times 20\,\mathrm{mm}^3$ LYSO:Ce crystals readout by Hamamatsu S8550 APD arrays. The APDs are optically coupled to both ends of the 6144 crystals in order to extract the DOI information for each detected event. Each one of 12288 APD's pixels is read and controlled by Application Specific Integrated Circuits water-cooled by an external cooling unit. The Clear-PEM frontend boards innovative design results in a unprecedented integration of the crystal matrices, APDs and ASICs, making Clear-PEM the PET scanner with the highest number of APD pixels ever integrated so far.

In this paper, the scanner's main technical characteristics, calibration strategies and the first spectrometric performance evaluation in a clinical environment are presented.

The first commissioning results show 99.7% active channels, which, after calibration, have inter-pixel and absolute gain distributions with dispersions of, respectively, 12.2% and 15.3%, demonstrating that despite the large number of channels, the system is uniform. The mean energy resolution at 511 keV is of 15.9%, with a 8.8% dispersion, and the mean C_{DOI}^{-1} is 5.9%/mm, with a 7.8% dispersion. The coincidence time resolution, at 511 keV, for a energy window between 400 and 600 keV, is 5.2 ns FWHM.

KEYWORDS: Gamma camera, SPECT, PET PET/CT, coronary CT angiography (CTA); Photon detectors for UV, visible and IR photons (solid-state) (PIN diodes, APDs, Si-PMTs, CCDs, EBCCDs etc); Front-end electronics for detector readout

[1] Corresponding author.

doi:10.1088/1748-0221/4/10/P10011

2009 JINST 4 P10011

Contents

1 Introduction

One in every eleven Portuguese women are diagnosed with Breast Cancer, which makes it one of the most common cancers and the leading cause of death by cancer for women between the ages of 35 and 55 [1]. This incidence rate value is similar to most developed countries. If diagnosed correctly and on its early stages, the 5-year relative survival rate is higher than 90%. However, the most common and wide-spread diagnostic technique, X-ray mammography, can only provide anatomical information of the breast tissues, resulting in a high false-positive rate, specially in dense breasts. There is therefore a great need for a breast cancer diagnosis system with both a high specificity and a high resolution. Positron Emission Tomography (PET) imaging [2], in which the Clear-PEM scanner is based, presents itself as a viable solution to this need.

PET whole-body scanners using ^{18}F-FDG as a radioactive tracer and dual-time-point imaging, have a sensitivity higher than 90% for breast tumors larger than 1 cm, but lesions with less than 1 cm in diameter can be undetected [3]. To solve this problem it is necessary to design PET scanners exclusively for breast imaging, known as Positron Emission Mammography scanners (PEM) [4, 5]. The Clear-PEM scanner was thus designed to have high sensitivity, high specificity and a good spatial resolution in order to detect small tumors, both on the breast and axilla regions [6, 7].

Unlike in common ring-shaped PET scanners, the Clear-PEM's detector plates are very close to each other, increasing the parallax effect [8]. This effect occurs when the interaction point of the photon that penetrates into the detector module is assigned to the front face of the detector element, introducing a mispositioning in the Line-of-Response (LOR). If the depth-of-interaction

2009 JINST 4 P10011

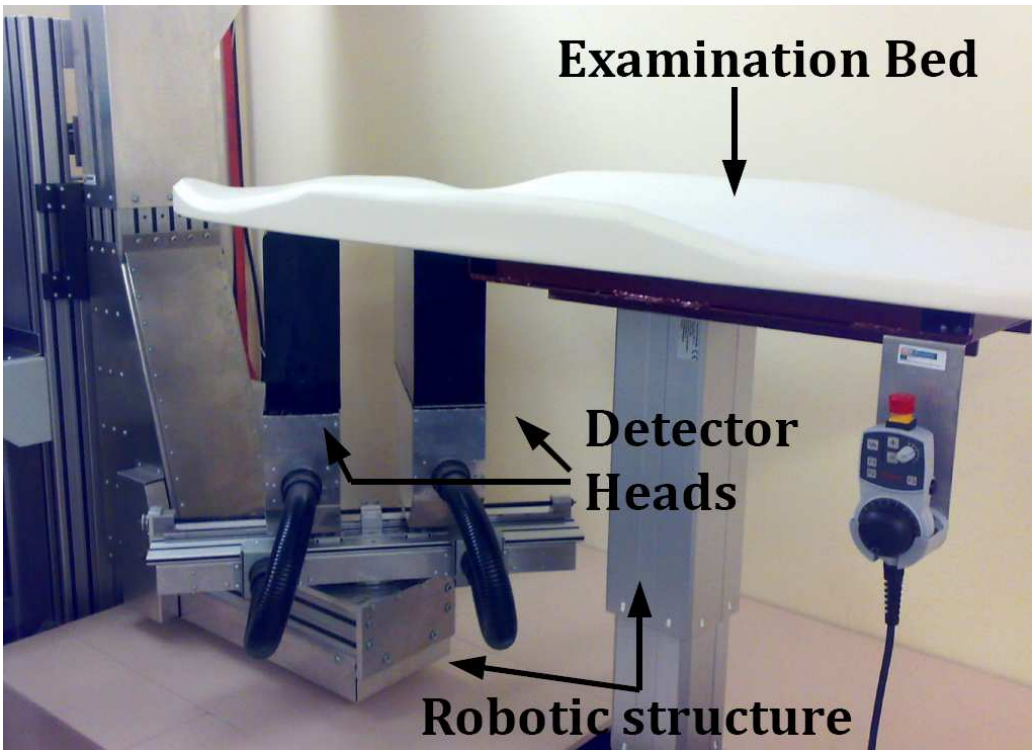

Figure 1. Photograph of the Clear-PEM scanner installed in the hospital.

(DOI) is measured, then the interaction point is no longer assigned to the front face and most of the positioning error is eliminated. In order to find a compromise between the parallax effect and detection sensitivity, a detector module with high-Z, fine pitch $2 \times 2 \times 20\,\mathrm{mm}^3$ LYSO:Ce crystals [9] and APDs optically coupled to both ends of the crystals, was chosen, allowing measuring the DOI of the incoming photons [10–12]. Also, very efficient data acquisition systems, with low dead-time, were implemented, enabling the full acquisition of the data generated during an exam [13].

The Clear-PEM scanner was installed at the *Instituto Português de Oncologia do Porto* hospital in December 2008 and the first clinical trials will occur during the year of 2009. Figure 1 shows the scanner at the hospital.

This paper mainly focuses on the spectrometric performance of the Clear-PEM tomograph in clinical environment, being the imaging performance discussed on another paper [10]. Section 2 contains a small overview of the scanner's main technical characteristics. The calibration strategy is briefly described on section 3. Section 4 presents the experimental results from the Clear-PEM integration phase in clinical environment. Section 5 presents the conclusions.

2 The Clear-PEM scanner

The Clear-PEM scanner is composed by two planar detector heads attached to a robotic arm, a trigger/data acquisition electronics system and a rack with the data acquisition and detector control system servers plus the low voltage and high voltage power supplies. The detector heads hold LYSO:Ce crystal matrices, with 32 $2 \times 2 \times 20\,\mathrm{mm}^3$ crystals each, and Hamamatsu S8550 APD pho-

2009 JINST 4 P10011

Table 1. Major technical specifications of the Clear-PEM scanner.

Number of LYSO:Ce crystals	6144 ($2 \times 2 \times 20\,mm^3$ each)
Number of crystal matrices	192
Number of electronic channels	12 288
Number of multi-pixel APDs	384
Number of multi-channel ASICs	64
Number of LORs	9 437 184
Scintillator volume	$491.52\,cm^3$ ($\approx 3.5\,kg$)
Active surface area	$18 \times 16\,cm^2$ (≈ 13 channels/cm^2)

tosensors that are read by highly integrated 192:2 Application Specific Integrated Circuits (ASIC) water-cooled by an external cooling unit, capable of keeping the temperature within the range of 17–19 °C with a stability of ±0.1 °C. Each acquisition performed by the ClearPEM scanner is made with the detector heads kept still.

In the ASIC, amplification, shaping, sampling, channel selection and analog multiplexing of the signal are performed. The output pulse dataframe is composed of 10 analog level samples which are then digitized by a free running ADC and sent to the off-detector electronics (L1 trigger), based on a FPGA fabric which implements temporary data storage and computation of trigger primitives (energy and time) and coincidence triggering. The selected data is then transfered to the next level trigger (L2 trigger), implemented in software.

The patients are placed on the prone position on the examination bed, which has an opening that allows the detector heads to access the breast to be examined. In order to ensure tomographic reconstruction, when one acquisition ends the detector heads are rotated by the robotic arm into a new position, where another acquisition occurs [10, 14]. The main technical parameters of the scanner are shown in table 1. Other details about the design and technical characteristics of the Clear-PEM scanner can be found on our previous papers [7, 12, 13, 15, 16].

3 Calibration methods

A correct energy calibration of all the channels is essential to correctly identify the photons that are coincident in time and originated by the same positron annihilation without undergoing Compton scattering on their way to the detector, by narrowing the time and energy acceptance windows. The use of a narrow coincidence window, together with an accurate event timing determination and low system dead-time, is required to minimize the presence of background random coincidence events, which, in PEM systems, are mainly due to the single photon events flux originated in the patient's torso. This background activity contributes to a contrast loss and introduction of artifacts in the reconstructed images. The DOI calibration is needed to obtain information about the interaction position of the photon with the crystal in order to minimize the Line-of-Response's positioning error [8].

Calibration strategies that allow for a fast calibration with minimum human participation are thus required for the scanner to be operated by hospital staff and integrated in normal clinical routine. The calibration methods are described briefly in the following subsections and a more detailed description can be found in [16–18].

2009 JINST 4 P10011

3.1 Energy calibration

The energy of every detected hit is given by the sum of the energies measured by the two APDs that readout the top and bottom ends of the crystal where the photon interacted. It is then required that both APDs have an equalized gain. Taking advantage of the natural presence of ^{176}Lu within the LYSO:Ce crystal, uniformly distributed along its entire volume, the inter-pixel gain is determined by assuming that the energy spectra of each APD should be the same. Taking as reference the top APD's spectrum, a K_{rel} constant is multiplied by the amplitude of the bottom APD signal. Once the gain of the APDs is equalized, the top-bottom summed spectrum can be calibrated in energy by finding the position of the 511 keV peak emitted by either a ^{68}Ge or a ^{22}Na source and computing the absolute gain constant K_{abs}. The energy of each event, in keV, is then estimated by:

$$E = K_{\text{abs}} \left(E_t + K_{\text{rel}} E_b \right) \tag{3.1}$$

where E_t and E_b are the values of the pedestal-subtracted pulse's amplitude of the top and bottom APDs, respectively.

To find the correct K_{rel}, the bottom and top APD spectrum for a single crystal are compared and a χ^2 distribution, that measures the similarity between the spectrum, is computed. This distribution's minimum value is then determined, corresponding to K_{rel}. The distribution is defined as [7, 19]:

$$\chi^2 = \sum_{i=1}^{N} \frac{\left(\psi_t^i - K_{\text{rel}} \psi_b^i \right)^2}{\psi_t^i + K_{\text{rel}} \psi_b^i} \tag{3.2}$$

where ψ_t^i and ψ_b^i are the number of entries in each i bin of the energy spectra of the top and bottom APD, respectively, and N is the total number of bins.

3.2 DOI calibration

The interaction depth of a photon, z, is computed from the asymmetry of light collection between the two APDs that readout the light of a given crystal by:

$$z = C_{\text{DOI}} \frac{E_t - K_{\text{rel}} E_b}{E_t + K_{\text{rel}} E_b} \tag{3.3}$$

The C_{DOI} constant transforms the ratio of shared light into a physical distance unit and is obtained right after K_{rel} calibration, also using the ^{176}Lu present in the crystal. This constant is then determined by finding the edges of the asymmetry distribution, which is uniform due to the uniform concentration of the ^{176}Lu decays along the crystal [20]. From this assumption, C_{DOI} is estimated by:

$$C_{\text{DOI}} = \frac{20 \text{ mm}}{(\text{Asymmetry at positive edge}) - (\text{Asymmetry at negative edge})} \tag{3.4}$$

where *Asymmetry at positive edge* and *Asymmetry at negative edge* are the asymmetry values on the corresponding crystal edges, extracted from a light collection asymmetry plot like the one shown in figure 13(b) [20].

2009 JINST 4 P10011

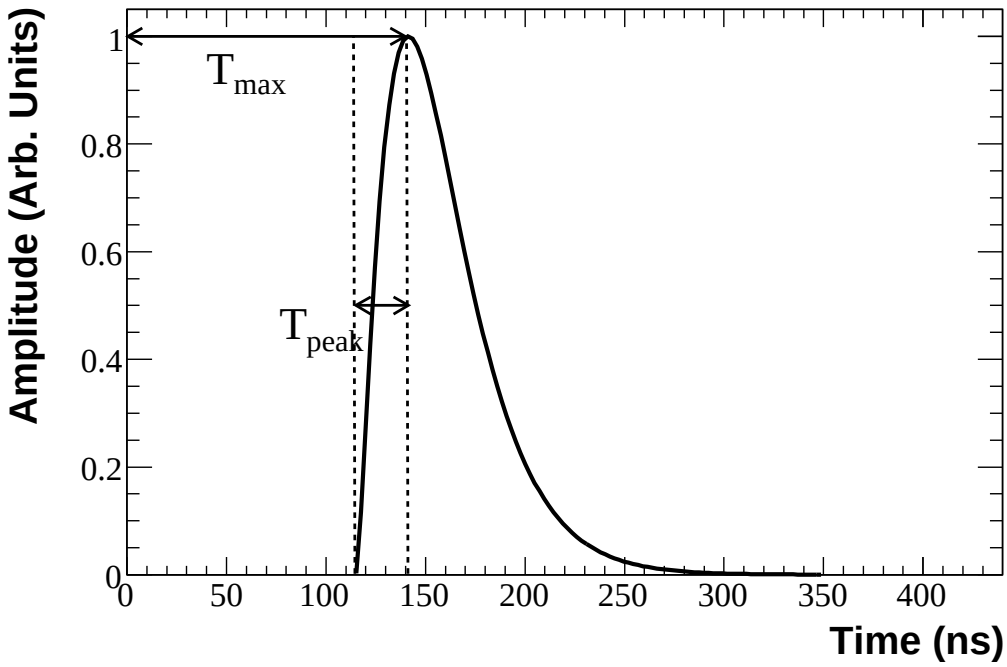

Figure 2. Pulse shape parameterization $f(t)$.

3.3 Time calibration

To discriminate between two photon events of the same decay from uncorrelated single photons from distinct decays, a PET system needs to be able to extract the time information from each interaction with a resolution of about a few nanoseconds [21, 22].

In Clear-PEM, after the APD signals arrive in the corresponding ASIC, the amplification, shaping, channel selection and analog multiplexing are performed (figure 3(a) shows the routing between a ASIC and its corresponding APDs). The pulse dataframe, seen on figure 4, is composed of 10 analog level samples which are then digitized and sent to the L1 trigger electronics. The selected data is then transfered to the Level 2 trigger, implemented in software.

A key assumption for the time extraction of each pulse is that the pulse shape for every APD/ASIC channel can be predetermined. Pulse reconstruction assumes that the individual response of each channel to a characteristic APD charge input can be parameterized by means of a generic function given by:

$$f(t) = A\left(\frac{t-(T_{\max}-T_{\text{peak}})}{T_{\text{peak}}}\right)^{\alpha} \exp^{-\alpha\left(\frac{t-T_{\max}}{T_{\text{peak}}}\right)} \tag{3.5}$$

where T_{peak} is the peaking time, α the form factor, $T_{\max}$ the absolute position of the maximum in respect to the sampling clock frequency (50 Mhz) and A the amplitude (see figure 2) [23]. The time of the pulse is defined as $T_{\max}$-T_{peak}. In the Level 1 trigger electronics, each pulse's pedestal, estimated from the first two samples, is subtracted from the pulse's dataframe and the pedestal-subtracted dataframe is fitted using $f(t)$ to estimate the phase δ_t, defined as:

$$\delta_t = T_{\max} - \text{MaxClock} \tag{3.6}$$

2009 JINST 4 P10011

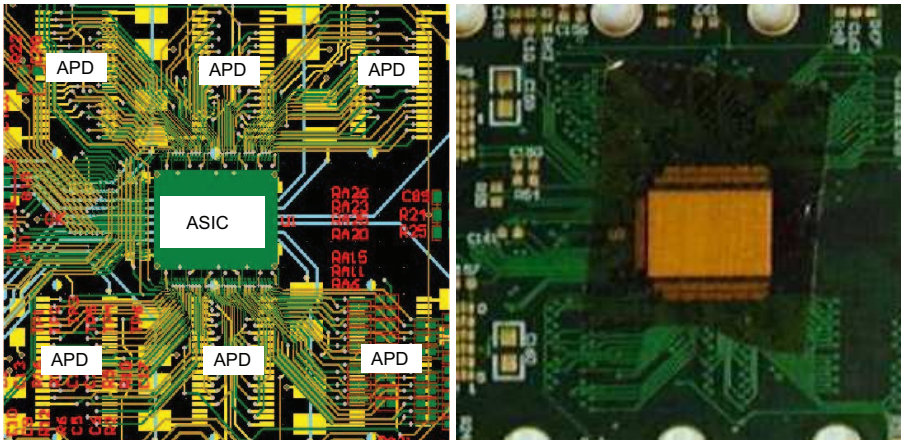

(a) (b)

Figure 3. Close-up schematic (a) and photo (b) of the bare PCB routing section between the ASIC and APDs in the frontend board (ASIC die not mounted).

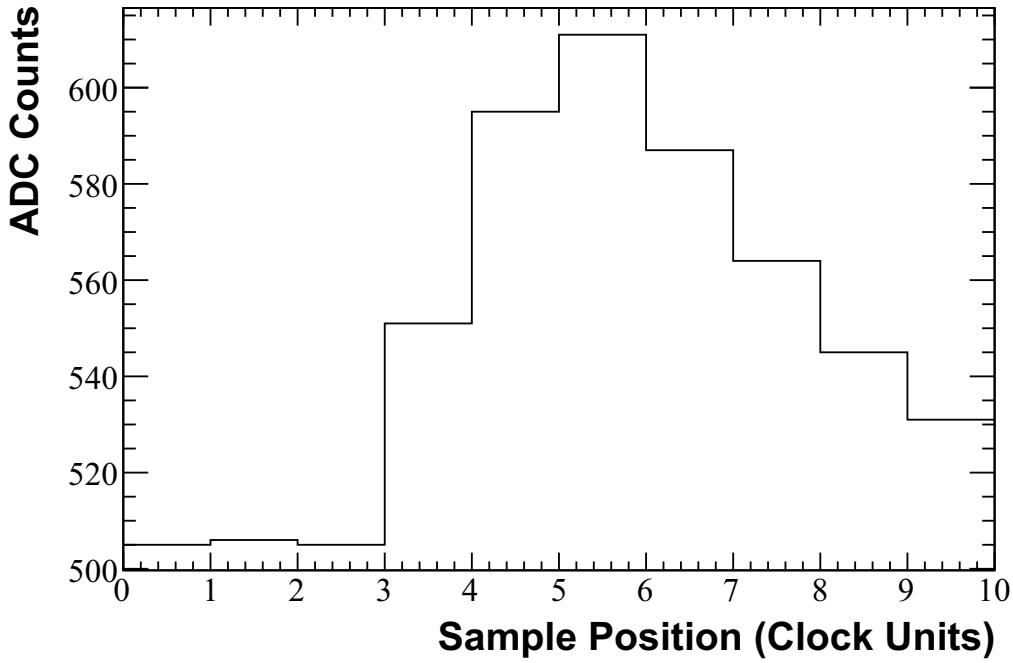

Figure 4. Typical pulse dataframe.

where MaxClock is the clock position of the highest sample in the dataframe. Each dataframe is then corrected by the phase and the samples are accumulated in a profile histogram built for each channel. The profile histograms are fitted by the Level 2 trigger calibration software, using the $f(t)$ function with variables $T_{\max}$, T_{peak} and α free during the minimization process. Since the pulse shape is normalized and pedestal-corrected, the parameter A is fixed to 1 [18].

2009 JINST 4 P10011

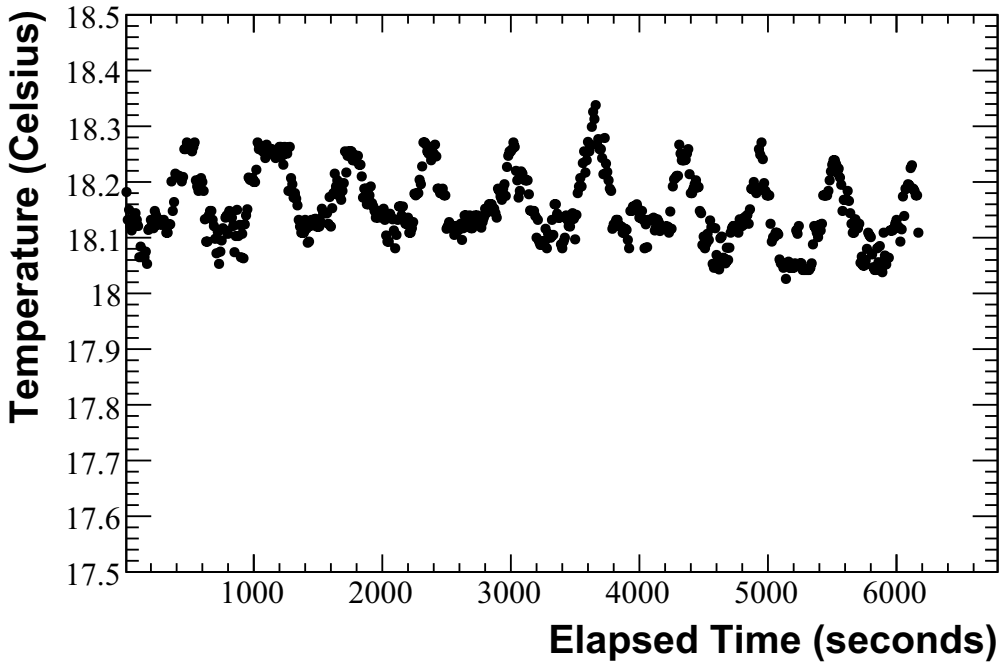

Figure 5. In-detector heads temperature evolution.

4 Experimental results from the Clear-PEM integration phase

The results presented in this section were obtained with the assembled scanner, having 75% of the total number of crystal matrices installed due to logistics-related time constraints, operating in a clinical environment, and using the ^{176}Lu background and an $160 \times 180\,\mathrm{mm}^2$ planar ^{68}Ge source, with both sources providing a rather uniform number of decays for all crystals. The obtained values are frequently compared with the results obtained during the ASIC characterization stage with the "Trigger Cell" setup, presented in a previous paper [16], where two ASIC chips were tested using a dedicated setup, basically composed by two small frontend boards (FEBs) coupled to six LYSO:Ce crystal arrays.

The APDs' gain has a dependence on temperature. With gain 100, at which the APDs are operated, the APDs' gain varies 4.0%/°C, so it is imperative that the temperature inside the ClearPEM detector heads is monitored and controlled in real time, which is done by means of a PT1000 readout [15]. The maximum relative deviation to the mean temperature value is less than 0.6% (see figure 5), the observed oscillations being caused by the water-cooling system's limited precision of 0.1 °C.

4.1 Noise measurements

Figures 6(a) and 6(b) show the distribution of mean pedestals, obtained by reprocessing in off-line mode the dataframes acquired by the L1 trigger. In order to evaluate if the top and bottom FEBs have similar behaviors, which is particularly critical with a double-readout architecture, and to detect structure-induced variations, the parameter's distribution is shown for the bottom and top boards, separately. The mean pedestal value, extracted from a gaussian fit, is 516 and 517

2009 JINST 4 P10011

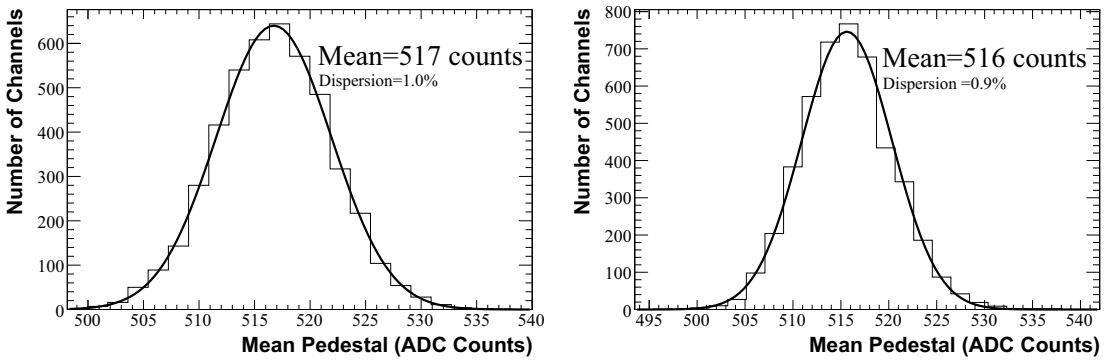

(a) (b)

Figure 6. Mean pedestal distribution for channels on the top (a) and bottom frontend boards (b).

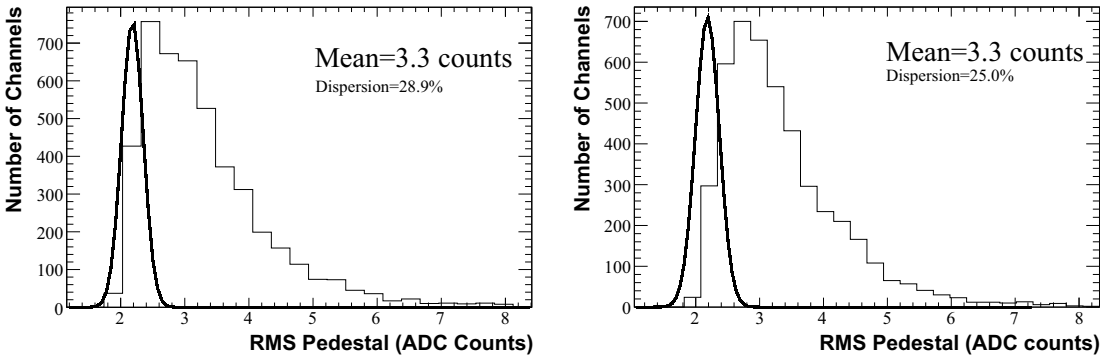

(a) (b)

Figure 7. RMS pedestal distribution for channels on the top (a) and bottom frontend boards (b). The thicker black line shows the noise distribution obtained with the ASIC characterization setup [16].

ADC counts[1] for the top and bottom FEBs, respectively, with dispersions[2] of 1.0% and 0.9% that guarantee a low inter-pixel pedestal variation and allow the use of low ASIC threshold voltage (which limits the minimum energy of a detectable event), common to all 192 channels inside each chip. These results are comparable to the ones obtained in the characterization stage of the ASIC, where a mean pedestal of 513 ADC counts and a dispersion of 0.5% were measured.

The distribution of the electronics noise, defined as the pedestal RMS, is shown in figures 7(a) and 7(b). Both the top and bottom boards' distributions don't follow a gaussian profile. The mean value of the noise, for both FEBs, is 3.3 ADC counts, with dispersions of 28.9% and 25.0% for the top and botttom FEBs, respectively. The results obtained from the ASIC characterization setup showed a mean noise of 2.2 ADC counts and a dispersion of 7.8%, being its normalized noise distribution represented on figures 7(a) and 7(b) by the thick black line [16]. In the assembled scanner, the noise distribution shows an increase on both the mean noise and dispersion values. These increases are caused by the very compact cabling inside the ClearPEM's detector heads,

[1] Differential 10-bit ADCs are used in the system.

[2] Defined as the relative standard deviation.

2009 JINST 4 P10011

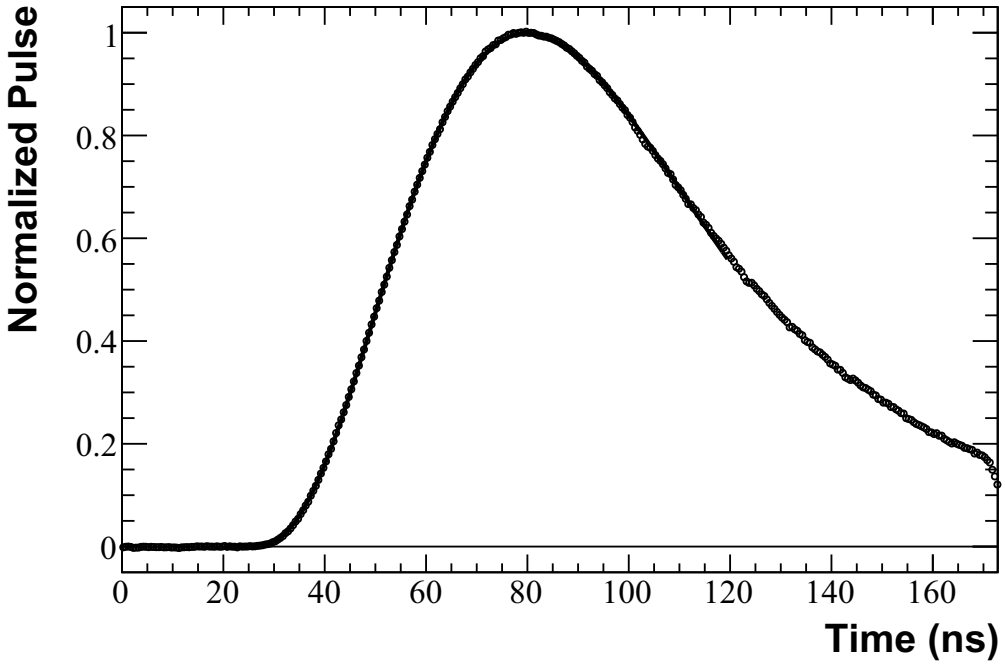

Figure 8. Typical reconstructed pulse for a single LYSO-APD-ASIC channel.

which induces more noise than the simpler ASIC characterization setup, due to electronic noise pickups and other parasitical effects [16]. It will be shown that this doesn't affect the energy and timing resolutions, as well as the ability to extract DOI information. Improvements in the next-generation FEB layout are expected to provide better immunity to noise pickup.

4.2 Pulse shape

In this section we present the results of the fit of the $f(t)$ to the profile histogram of all channels in the system.

A typical reconstructed pulses' profile histogram, as described in subsection 3.3, is shown on figure 8. The T_{peak} distributions on the bottom and top boards are shown in figures 9(a) and 9(b). It is possible to clearly identify a group of faster channels, corresponding to ASIC blocks that are faster due to differences in the production process. Not considering these faster channels, one can say that both the bottom and top boards have similar mean values of 58.9 ns and 59.1 ns, respectively, yielding a common dispersion of 1.9%. These results are compatible with the ones obtained with the ASIC characterization setup, where a mean T_{peak} value of 57.2 ns and a dispersion of 1.9% was measured [16].

The α distributions are presented in figures 10(a) and 10(b). Again, it is possible to identify a group of channels that correspond to ASIC blocks with different characteristics. Not considering these blocks, the obtained mean value and dispersion for both the top and bottom boards, extracted from a gaussian fit, are 3.6% and 3.8%, respectively. These values are in good agreement with the ones measured with the ASIC characterization setup, where a mean α of 3.5 and a dispersion of 2.9% were obtained [16].

2009 JINST 4 P10011

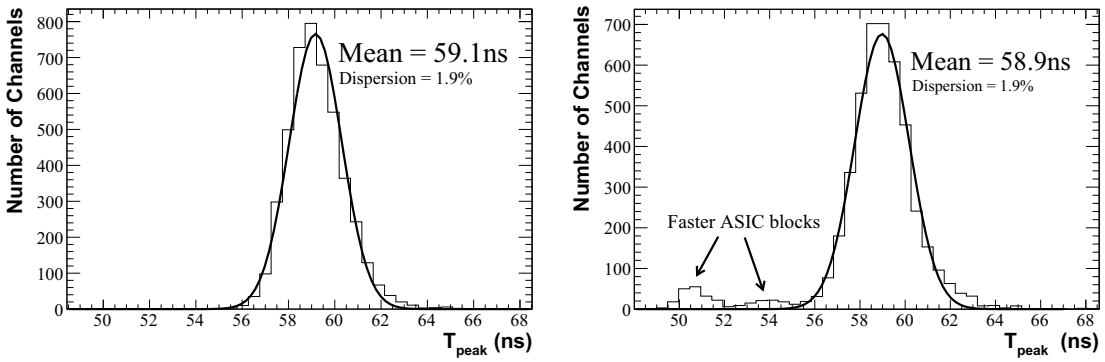

(a) (b)

Figure 9. Pulse shape parameters: peaking time T_{peak} as function of the channel on the top (a) and bottom frontend boards (b).

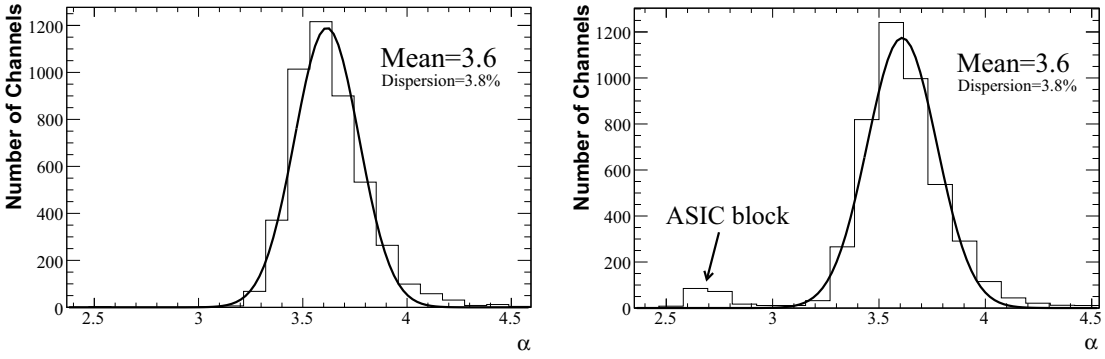

(a) (b)

Figure 10. Pulse shape parameters: α parameter as function of the channel on the top (a) and bottom frontend boards (b).

The time calibration can be further analyzed by taking the sampling clock as reference and analyzing the δ_t distribution, defined in Subsection 3.3. Figures 11(a) and 11(b) show the δ_t distributions of the pulses of events with energies higher than 250 keV, which, as expected [22], are relatively flat in the -0.5 to 0.5 clocks range, due to the randomness of the positron annihilation events and corresponding lack of correlation with the sampling clock. A limited region with phase differences close to zero has higher counts than expected. This issue is currently under investigation.

4.3 Time resolution

The coincidence time resolution for 511 keV photons, defined as the FWHM of the gaussian fit of the distribution of the time difference between 2 photons originated from the same positron decay, using a 400–600 keV energy window and considering all possible coincidence LORs in the system, is of 5.2 ns, as shown in figure 12. It should be noted that this time resolution value was obtained using only the calibration methods described earlier. Time shifts due to the propagation of delays introduced by differences in the dynamic response of LYSO:Ce-APD readout and signal

2009 JINST 4 P10011

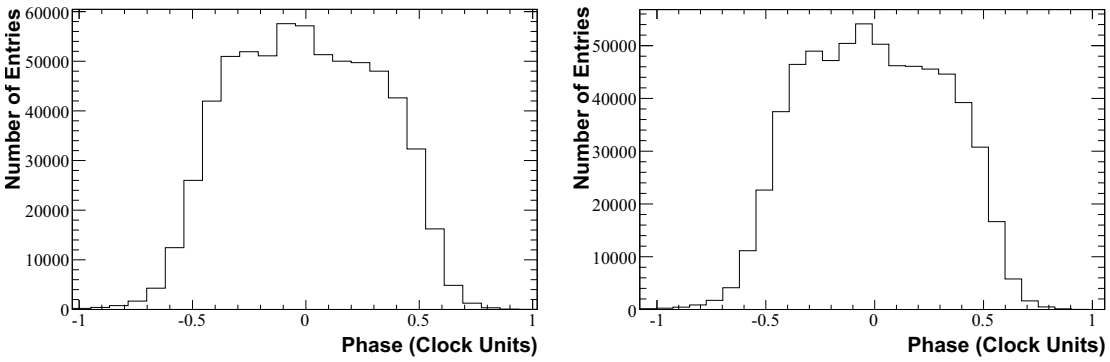

(a) (b)

Figure 11. Events over 250 keV pulse's phase (in reference to the sampling clock) distribution on the top (a) and bottom frontend boards (b).

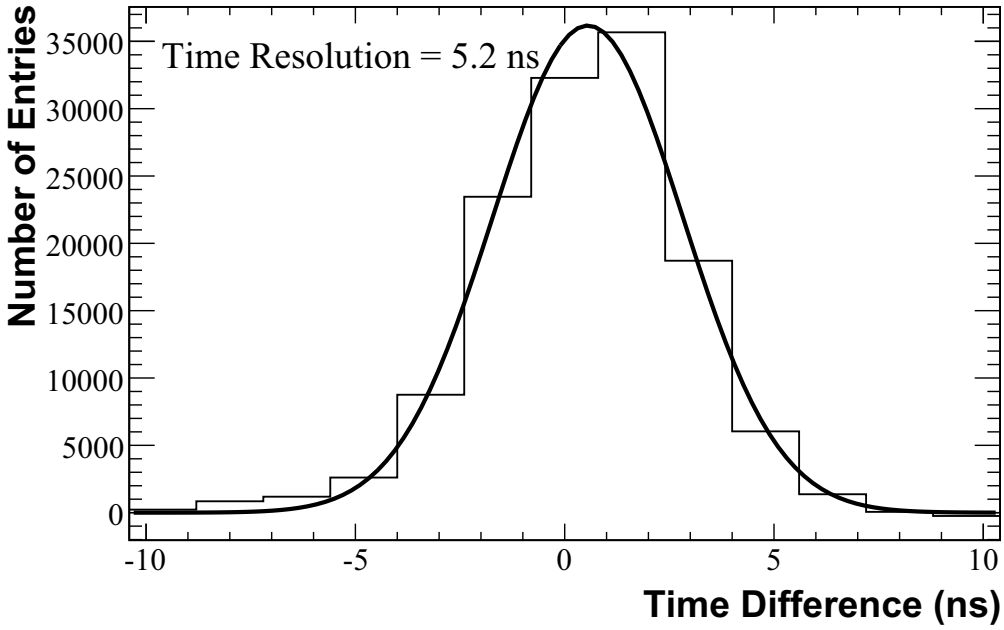

Figure 12. Background-subtracted distribution of the measured time differences between the detection of photons originated by the same positron decay.

propagation in the PCBs were not corrected. Thus, it can be expected that a better FWHM time resolution can be obtained through improvements in the calibration procedures. Still, such a low value for a compact, dual-readout APD-based system, is the result of the very low noise level achieved in the developed frontend electronics and the careful optimization of the detector modules, being comparable or better than the time resolution of some PMT-based scanners [21, 24] and most APD-based detectors [25, 26].

2009 JINST 4 P10011

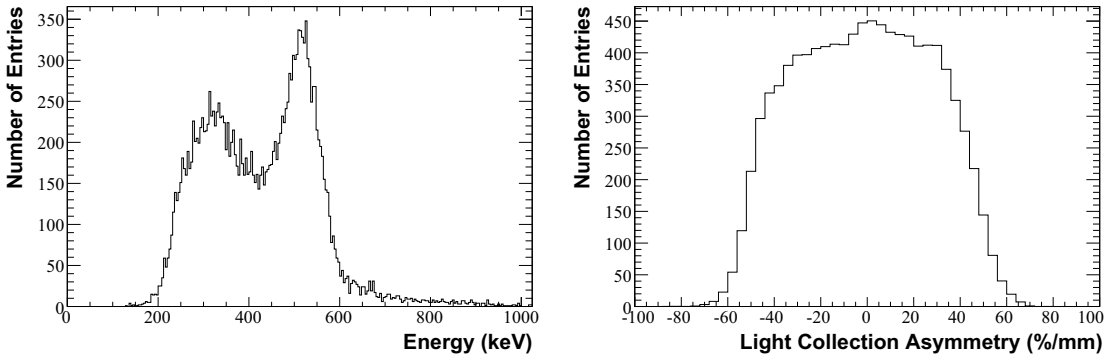

(a) (b)

Figure 13. Typical energy spectrum for a single crystal of a ^{68}Ge acquisition run (a) and light collection asymmetry between the two pixel APDs coupled the same crystal, for a ^{176}Lu background acquisition run (b).

4.4 Energy measurements

Data was analyzed off-line for the determination of detector's calibration (K_{rel}, K_{abs} and C_{DOI}^{-1} for each crystal), necessary for the measurement of the individual energy spectra and light collection asymmetry distributions. A typical LYSO:Ce crystal ^{68}Ge energy spectrum and light collection asymmetry distribution for ^{176}Lu are shown in figures 13(a) and 13(b). The energy resolution ($2.35\Delta E/E \times 100\%$) at 511 keV of a given spectra is extracted from a Gaussian fit after Compton background subtraction through ROOT's TSpectrum background estimation function [27, 28].

Figure 14(a) shows the K_{rel} inter-pixel calibration constant distribution, which yields a mean value of 1.0 and a dispersion of 12.2%. This dispersion value is in good agreement with the predicted value of 13% [11].

The absolute gain distribution, shown in figure 14(b), yields a mean value and dispersion of, respectively, 2.3 keV/ADC and 15.1%, being this dispersion value similar to the one obtained with the ASIC characterization setup, of 13.0% [16].

The C_{DOI}^{-1} distribution is presented on figure 14(c), having a mean value of 5.9%/mm and a dispersion of 7.8%, obtained from a gaussian fit. Once again, these results follow the ones obtained with the ASIC characterization setup, when the measured mean C_{DOI}^{-1} value and dispersion of the distribution were 5.9%/mm and 8.0%, respectively [16].

The distribution of the energy resolution at 511 keV for all channels is shown in figure 14(d), presenting a mean value of 15.9% and a dispersion of 9.1%, extracted from a gaussian fit. These results are similar to the 15.6% energy resolution and 7.6% dispersion obtained with the ASIC characterization setup [16].

The influence of the DOI of the detected photons on the energy resolution was investigated by dividing the crystals in five 4 mm bins along the longitudinal axis and analyzing the resulting spectra's energy resolution. The data for eleven crystals is shown in figure 15. The average energy resolution of the full spectra of the analysed crystals is of 15.4%. The DOI bins have a higher and more disperse mean energy resolution value the farther away the events' DOI coordinate is from the crystal center. For all the analyzed crystals, the full crystal spectrum's energy resolution is worse than at least three of the five 4 mm bins spectra's energy resolution. This can be justified by a slight

2009 JINST 4 P10011

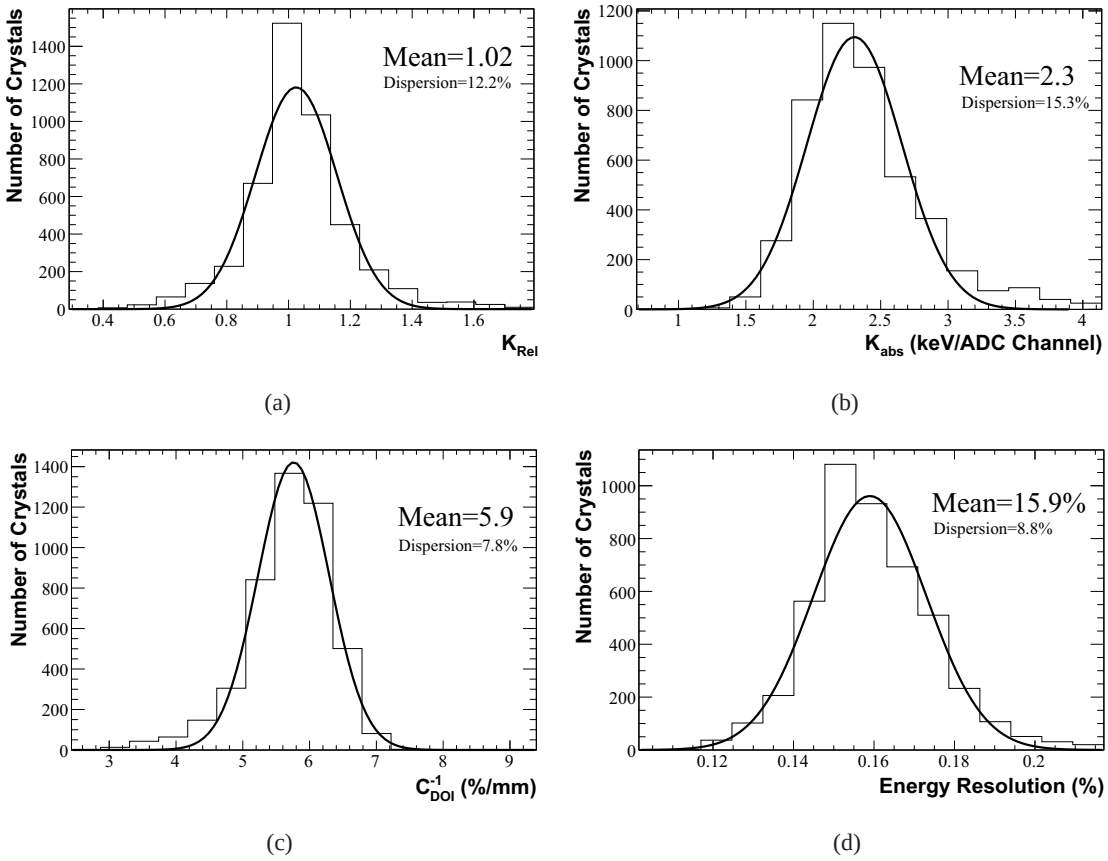

Figure 14. K_{abs} (a), K_{rel} (b), C_{DOI}^{-1} (c), and energy resolution at 511 keV (d) as function of the channel.

variation of the 511 keV peak position with the DOI, which can be observed in figure 16 that shows the 511 keV peak position (normalized to the average peak position), determined by using ROOT's Search algorithm [29], as a function of the DOI coordinate, where the maximum relative variation of the peak position is of 1.4%.

Figure 17 shows the distribution of the 511 keV peak position of the calibrated spectra, again determined by using ROOT's Search algorithm [29]. The mean value of the peak's position, extracted from a gaussian fit, is 511.8 keV with a dispersion of 0.8%, confirming the overall calibration quality and the absolute gain calibration's validity in particular.

The sum of the spectra of all crystals, before and after the detector's calibration, are shown, respectively, in figure 18(a) and figure 18(b). It is difficult to identify the 511 keV peak from the summed uncalibrated spectra plot, but this peak is clearly recognizable on the summed calibrated spectra plot. Adding the fact that the energy resolution at 511 keV of the summed calibrated spectra is 16.0%, being very close to the mean value of the energy resolution distribution showed in figure 14(d), the validity of the calibration performed is again confirmed. One can also conclude that the despite the double-readout configuration decreases the ammount of collected light, it is possible to obtain an energy resolution similar or better than those obtained with single-readout schemes with multi-anode PMTs or multi-pixel APDs systems [21, 24, 26].

2009 JINST 4 P10011

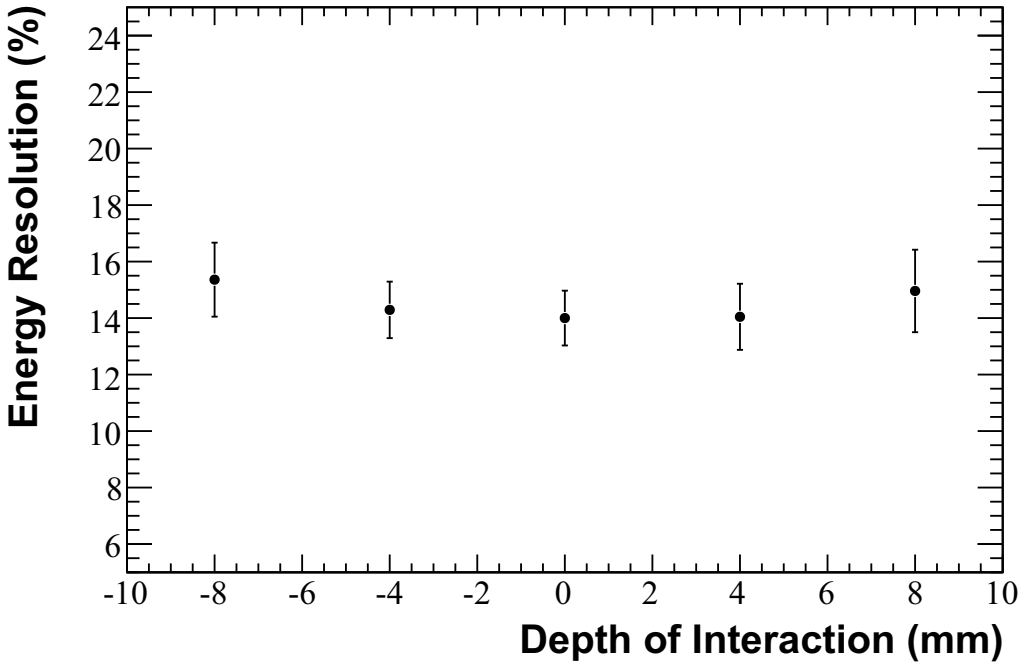

Figure 15. Average energy resolution at 511 keV as function of the DOI coordinate, for 11 crystals.

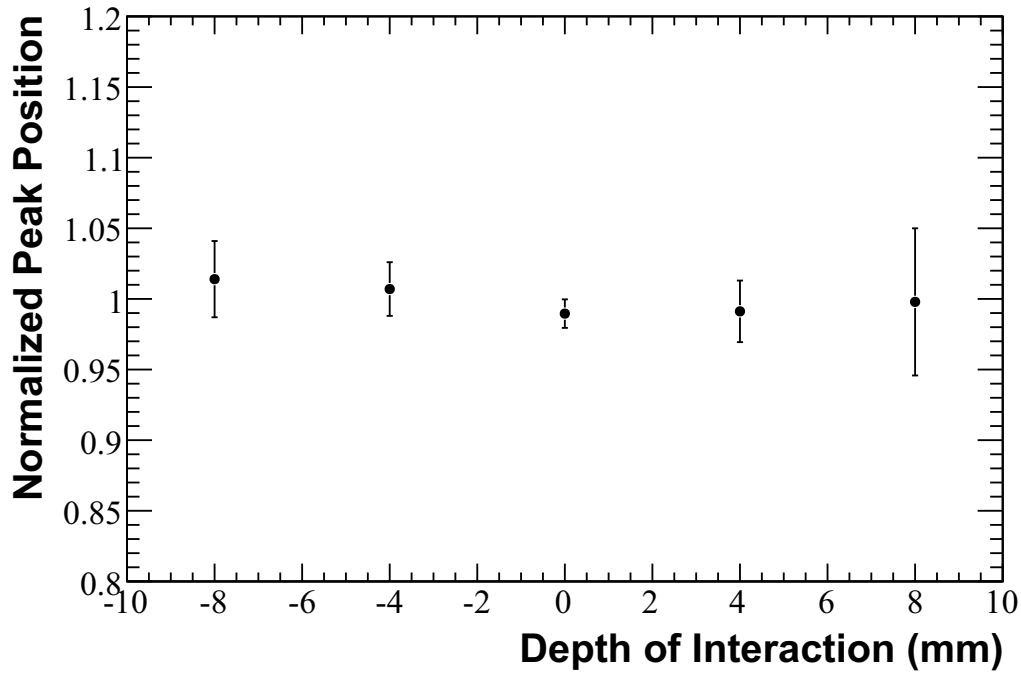

Figure 16. Average 511 keV peak position as function of the DOI coordinate, for 11 crystals.

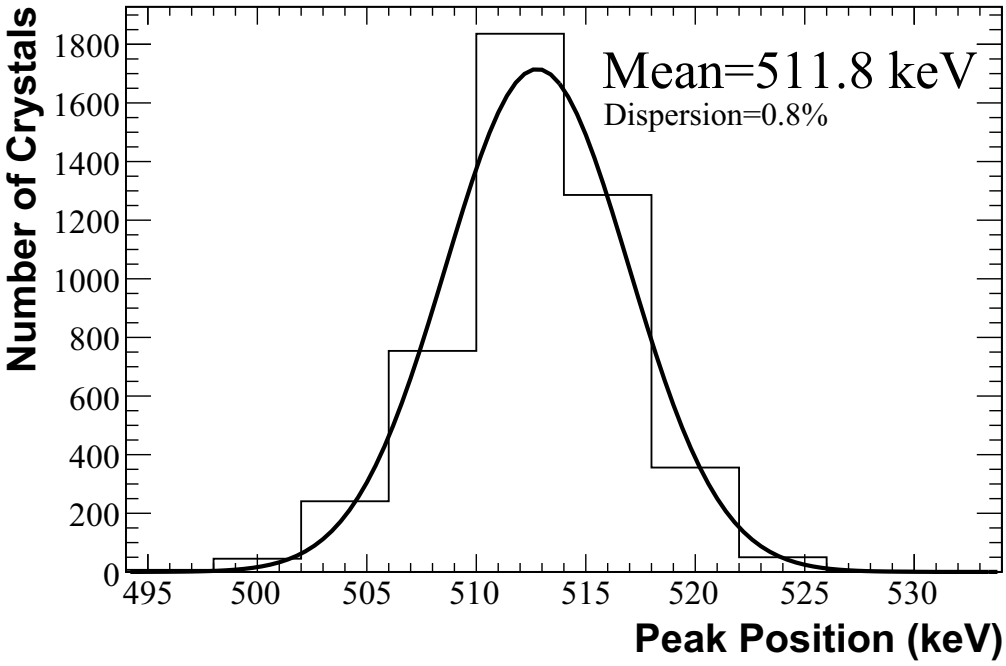

Figure 17. Calibrated spectra's 511 keV peak position distribution.

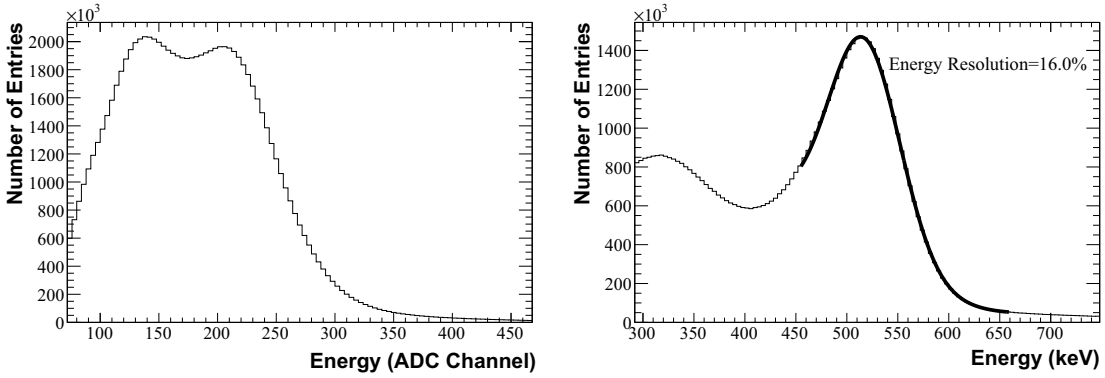

(a) (b)

Figure 18. Summed spectra of all crystals: before calibration (a) and after calibration (b).

In the top-bottom event energy scatter plot shown in figure 19, one can clearly distinguish the Compton and 511 keV peaks. The 511 keV region shows a greater number of high energy events read by the bottom APDs, which can be explained by the fact that most of the photons will interact near a crystal's bottom face as this one is closer to the radiation source. The presence of Compton background on the 511 keV peak, seen in figure 18(b), shows itself as the bowed line bounding this peak's region.

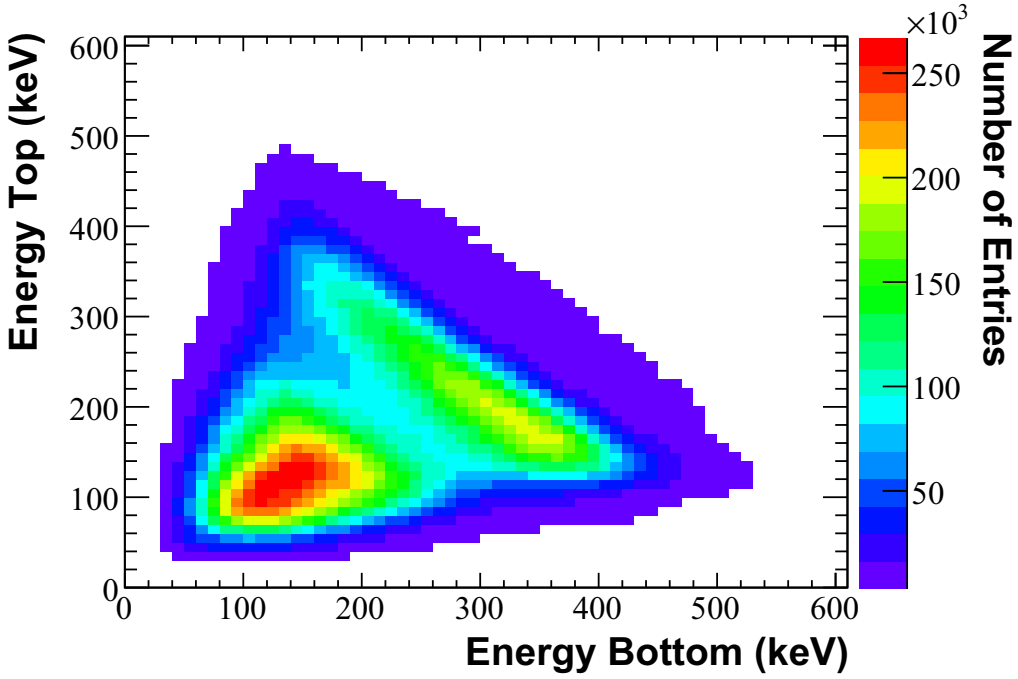

Figure 19. Top vs. bottom event energy scatter plot.

5 Conclusions

The Clear-PEM scanner has been recently installed in a hospital and its spectrometric performance was presented in this paper. Although the analysed data was obtained with 75% of the total number of crystal matrices, there should be no significant difference between the results presented in this paper and the ones obtainable with 100% of the crystal matrices installed.

The commissioning results show a uniform light collection for a uniform irradiation, 0.3% dead channels, 15.9% energy resolution at 511 keV with a 8.8% dispersion and a FWHM coincidence time resolution of 5.2 ns. As demanded, this allows for a precise identification of positron annihilation coincidence events. The inter-pixel and absolute gains are, respectively, 1.0 and 2.3 keV/ADC, with dispersions of 12.2% and 15.3%.

It was shown that the optimization carried out to extract DOI information, while enabling better reconstructed images, does not compromise the overall energy and time resolution, which are similar or better than PET systems based in PMT-readout.

In summary, an unprecedented integration of a large number of APD channels in high gain and compact, low noise frontend boards was achieved, together with the successful development of a mechanically maneuverable structure, data acquisition electronics plus detector control and safety systems.

During the commissioning, the first images were obtained and their quality, plus the overall imaging performance, will be discussed in a future paper [10].

2009 JINST 4 P10011

Acknowledgments

The authors would like to thank colleagues from the Portuguese PET Consortium and the Crystal Clear Collaboration for their suggestions and contribution. The Clear-PEM project is financed by AdI (Agência de Inovação) and FCT/POSI (Programa Operacional Sociedade da Informação), Portugal. The work of C. S. Ferreira, P. Rodrigues and A. Trindade was supported by FCT (Fundação para a Ciência e Tecnologia) under grants SFRH/BD/31646/2006, SFRH/BD/47448/2008, SFRH/BPD/37233/2007 and SFRH/BPD/37226/2007. The work of R. Bugalho, B. Carriço, C. Ortigão, J. F. Pinheiro, M. Frade, R. Moura, I. Rolo and R. Silva was supported by AdI.

References

[1] Laço, *Sobre o Cancro da Mama*, website http://www.laco.pt/layout1.php?p=2 (2008).

[2] L. Tafra, *Positron Emission Tomography (PET) and Mammography (PEM) for breast cancer: importance to surgeons*, *Ann. Surg. Oncol.* **14** (2007) 3.

[3] A. Mavi et al., *Dual Time Point ^{18}F-FDG PET Imaging Detects Breast Cancer with High Sensitivity and Correlates Well with Histologic Subtypes*, *J. Nucl. Med.* **47** (2006) 1440.

[4] W.W. Moses et al., *PET camera designs for imaging breast cancer and axillary node involvement*, *J. Nucl. Med.* **36** (1995) 69P.

[5] C.J. Thompson, K. Murthy , I.N. Weinberg and F.W. Maki, *Positron Emission Mammography (PEM): a promising technique to detect breast cancer*, *IEEE Trans. Nucl. Sci.* **42** (1995) 1012.

[6] P. Lecoq and J. Varela, *Clear PEM, A dedicated PET camera for mammography*, *Nucl. Instrum. Meth.* **A 486** (2002) 1.

[7] M.C. Abreu et al., *Design and evaluation of the Clear-PEM scanner for positron emission mammography*, *IEEE Trans. Nucl. Sci.* **53** (2006) 71.

[8] A. Trindade, *Design and evaluation of a Positron Emission Tomograph for breast cancer imaging*, Ph.D. Thesis, Instituto Superior Técnico, Portugal (2007).

[9] L. Pidol et al., *High efficiency of lutetium silicate scintillators Ce-doped LPS, and LYSO crystals*, *IEEE Trans. Nucl. Sci.* **51** (2004) 1084.

[10] A. Trindade et al., *Study of the influence of depth-of-interaction on Positron Emission Mammography images*, to be submitted to *JINST*.

[11] P. Amaral et al., *Performance and quality control of Clear-PEM detector modules*, *Nucl. Instrum. Meth.* **A 580** (2007) 1123.

[12] C. Ortigão et al., *Long-term stability of the Clear-PEM detector modules*, *Nucl. Instrum. Meth.* **A 571** (2007) 488.

[13] E. Albuquerque et al., *The Clear-PEM electronics system*, *IEEE Trans. Nucl. Sci.* **53** (2006) 2704.

[14] M. Martins, *3D Image Reconstruction for a Dual Plate Positron Emission Tomograph: Application to Mammography*, Ph.D. Thesis, Universidade de Lisboa, Portugal (2007).

[15] B. Carriço et al., *Characterization and quality control of avalanche photodiode arrays for the Clear-PEM detector modules*, *Nucl. Instrum. Meth.* **A 576** (2006) 19.

[16] E. Albuquerque et al., *Experimental characterization of the 192 channel Clear-PEM frontend ASIC coupled to a multi-pixel APD readout of LYSO:Ce crystals*, *Nucl. Instrum. Meth.* **A 598** (2009) 802.

2009 JINST 4 P10011

[17] J.F. Pinheiro, *Development and study of the Detector Control System and calibration software for the Clear-PEM Scanner*, Master Thesis, *Instituto Superior Técnico*, Portugal (2008).

[18] P. Bento et al., *Performance simulation studies of the Clear-PEM DAQ/Trigger system*, *IEEE Trans. Nucl. Sci.* **53** (2006) 2102.

[19] M.C. Abreu et al., *First experimental results with the Clear-PEM detector*, in proceedings of *2005 IEEE Nuclear Science Symposium and Medical Imaging Conference*, San Juan Puerto Rico, October 23–29 2005, *IEEE Nucl. Sci. Symp. Conf. Rec.* **3** (2005) 5.

[20] G.-C. Wang, J.S. Huber, W.W. Moses, W.-S. Choong and J.S. Maltz, *Calibration of a PEM detector with depth-of-interaction measurement*, *IEEE Trans. Nucl. Sci.* **51** (2004) 775.

[21] G.-C. Wang, J.S. Huber, W.W. Moses, J. Qi and W.-S. Choong, *Characterization of the LBNL PEM Camera*, *IEEE Trans. Nucl. Sci.* **53** (2006) 1129.

[22] P. Rodrigues, *Study and development of the Clear-PEM trigger and data acquisition system*, Ph.D. Thesis, Instituto Superior Técnico, Portugal (2007).

[23] CMS collaboration, P. Busson, *Digital Filtering for ECAL trigger primitives generator*, CMS-NOTE-1999-020 (1999).

[24] P.S. Roldan et al., *Performance evaluation of Raytest ClearPET, a PET scanner for small and medium size animals*, in proceedings of *2007 IEEE Nuclear Science Symposium and Medical Imaging Conference*, Honolulu Hawaii, U.S.A., October 27 – November 3 2007, *IEEE Nucl. Sci. Symp. Conf. Rec.* **4** (2007) 2859.

[25] M. Bergeron et al., *Performance evaluation of the LabPET APD-based digital PET scanner*, *IEEE Trans. Nucl. Sci.* **56** (2009) 10.

[26] D.P. McElroy et al., *Characterization and readout of MADPET-II detector modules: validation of a unique design concept for high resolution Small Animal PET*, *IEEE Trans. Nucl. Sci.* **55** (2005) 199.

[27] F. Brun and F. Rademakers, *ROOT: An object-oriented data analysis framework*, *Nucl. Instrum. Meth.* **389** (1997) 81 [*Linux J.* **51** (1998)].

[28] M. Morhac, J. Kliman, V. Matousek, M. Veselsky and I. Turzo, *Background elimination methods for multidimensional coincidence γ-ray spectra*, *Nucl. Instrum. Meth.* **A 401** (1997) 113.

[29] M. Morháč et al., *Identification of peaks in multidimensional coincidence gamma-ray spectra*, *Nucl. Instrum. Meth.* **A 443** (2000) 108.

2009 JINST 4 P10011